

ALMA follow-up of $\sim 3,000$ red-Herschel galaxies: the nature of extreme submillimeter galaxies.

Mariana Quirós-Rojas,^{1*} Alfredo Montaña,¹ Jorge A. Zavala,² Itziar Aretxaga,¹ and David H. Hughes¹.

¹*Instituto Nacional de Astrofísica Óptica y Electrónica, Luis Enrique Erro 1, Tonantzintla CP 72840, Puebla, México*

²*National Astronomical Observatory of Japan, 2-21-1 Osawa, Mitaka, Tokyo 181-8588, Japan*

Accepted XXX. Received YYY; in original form ZZZ

ABSTRACT

We present the analysis of over 3,000 red-*Herschel* sources ($S_{250\mu\text{m}} < S_{350\mu\text{m}} < S_{500\mu\text{m}}$) using public data from the ALMA archive and the *Herschel*-ATLAS survey. This represents the largest sample of red-*Herschel* sources with interferometric follow-up observations to date. The high ALMA angular resolution and sensitivity ($\theta_{\text{FWHM}} \sim 1$ arcsecond; $\sigma_{1.3\text{mm}} \sim 0.17$ mJy beam⁻¹) allow us to classify the sample into individual sources, multiple systems, and potential lenses and/or close mergers. Interestingly, even at this high angular resolution, 73 per cent of our detections are single systems, suggesting that most of these galaxies are isolated and/or post-merger galaxies. For the remaining detections, 20 per cent are classified as multiple systems, 5 per cent as lenses and/or mergers, and 2 per cent as low- z galaxies or Active Galactic Nuclei. Combining the *Herschel*/SPIRE and ALMA photometry, these galaxies are found to be extreme and massive systems with a median star formation rate of $\sim 1,500 M_{\odot}\text{yr}^{-1}$ and molecular gas mass of $M_{\text{gas}} \sim 10^{11} M_{\odot}$. The median redshift of individual sources is $z \approx 2.8$, while the likely lensed systems are at $z \approx 3.3$, with redshift distributions extending to $z \sim 6$. The inferred depletion times are consistent with the starburst-type population with a mild redshift evolution. Our results suggest a common star-formation mode for extreme galaxies across cosmic time, likely triggered by close interactions or disk-instabilities. Moreover, all galaxies with $S_{1.3\text{mm}} \geq 13$ mJy are gravitationally amplified which, similar to the established $S_{500\mu\text{m}} > 100$ mJy threshold, can be used as a simple criterion to identify gravitationally lensed galaxies.

Key words: submillimetre: galaxies – galaxies: high-redshift – galaxies: star formation – galaxies: starburst – surveys

1 INTRODUCTION

Early observations conducted by the *Infrared Astronomical Satellite* (*IRAS*), even limited to the low-redshift universe ($z \lesssim 0.1$), managed to show that astronomical objects emit an amount of energy in the infrared (IR) and sub-millimeter (submm) regime similar (or even higher) to that observed at ultraviolet (UV) and optical wavelengths. This result made evident the potential biases of surveys of the star formation activity in the universe due to the presence of embedded stars in areas with great abundances of dust and gas (Casey et al. 2014). Later, a population of high redshift galaxies whose infrared emission is dominated by dust heated by young stars, that contribute significantly to the IR and submm emission in the Universe, was confirmed. These sources, first found in maps of a few square arcminutes, were called Submillimeter Galaxies (SMG) (e.g. Smail et al. 1997; Hughes et al. 1998).

The SMG are characterized by having infrared luminosities (L_{IR}) of $\gtrsim 10^{12} L_{\odot}$, equivalent to those of Ultra-luminous infrared galaxies (ULIRGs) and even reaching the extreme luminosities of Hyper-luminous infrared galaxies (HyLIRGs, $L_{\text{IR}} \gtrsim 10^{13} L_{\odot}$). These luminosities correspond to star formation rates (SFR) of $\gtrsim 100 - 1,000 M_{\odot}\text{yr}^{-1}$. Some spectroscopic studies have probed the

CO line emission in this population, finding, typically, large reservoirs of molecular gas ($M_{\text{gas}} > 10^{10} M_{\odot}$) distributed in a varied morphology that includes disk galaxies and compact star formation bursts of gas-rich galaxies in interaction (e.g. Oteo et al. 2016). The inferred depletion times from these observations are at the order of tens of Myrs, which is short compared to the ~ 1 Gyr depletion time in normal galaxies (e.g. Tacconi et al. 2010; Saintonge et al. 2011). This difference opens the question of what is triggering the SFR in these galaxies, the high content of molecular gas or physical processes that are different in the early universe (see reviews by Blain et al. 2002; Carilli & Walter 2013; Casey et al. 2014).

Initially, studies such as Chapman et al. (2005) used optical spectroscopic observations to characterize the redshift distribution of 73 SMG, which had a median of $z = 2.2$. However, the spectroscopy of these sources required very long integration times and that placed a limit on how many galaxies could be studied. Moreover, these relatively small samples were considerably affected by biases at the highest redshifts ($z > 4$) introduced by the lack of detections at radio wavelengths, which at the time led to not having a good estimate of their position for spectroscopic follow up. Studies such as Aretxaga et al. (2005, 2007) and Yun et al. (2012), using multi-wavelength photometry in different fields such as Lockman Hole East (LH), SXDF and GOODS-S, also found that the redshift distribution of this population of galaxies has a median value between 2 and 3, with a small

* E-mail: mquiros@inaoe.mx

deviation between different works. However, these studies were carried out with dozens or at most just over a hundred galaxies in areas of square arcminutes. More recent studies using medium-to-large sample sizes of up to hundreds SMG (e.g. [DaCunha et al. 2015](#); [Miettinen et al. 2017](#); [Dudzevičiūtė et al. 2020](#)), found similar redshift distributions with median values between 2 and 3. The identification of significantly larger samples of extreme SMG at high redshift requires of surveys over larger areas of hundreds of square degrees.

The *Herschel* Astrophysical Terahertz Large Area Survey (*H-ATLAS*) is one of the largest projects in time and spatial coverage that was carried out with the *Herschel Space Observatory* (*Herschel*), covering ~ 600 square degrees of the sky towards the Galaxy And Mass Assembly (GAMA), North Galactic Pole (NGP) and South Galactic Pole (SGP) fields. This key project includes continuum observations with PACS (at $100\ \mu\text{m}$ and $160\ \mu\text{m}$) and SPIRE (at $250\ \mu\text{m}$, $350\ \mu\text{m}$ and $500\ \mu\text{m}$) ([Eales et al. 2010](#)). Galaxies with flux densities increasing from $250\ \mu\text{m}$ to $500\ \mu\text{m}$ ($S_{250\ \mu\text{m}} < S_{350\ \mu\text{m}} < S_{500\ \mu\text{m}}$) can be associated with SMG at $z > 2^1$ ([Hughes et al. 2002](#)). These galaxies have been called “*500 μm risers*” ([Pope & Chary 2010](#); [Cox et al. 2011](#)), and are also known as red-*Herschel* sources.

Using the first data release of the *H-ATLAS* collaboration, [Ivison et al. \(2016\)](#) identified a sample of 7,961 red sources detected above the 3.5σ threshold at $500\ \mu\text{m}$ and with flux ratios of $S_{500\ \mu\text{m}}/S_{250\ \mu\text{m}} \geq 1.5$ and $S_{500\ \mu\text{m}}/S_{350\ \mu\text{m}} \geq 0.85$. After a visual inspections of 2725 galaxies, a subsample of ~ 100 was drawn to be targeted with the James Clerk Maxwell Telescope and the Atacama Pathfinder Experiment. Subsequent studies and follow up observations have focused on these galaxies and have allowed to spectroscopically confirm and study some of the most distant and most extreme SMG that are known to date (e.g. [Ivison et al. 2016](#); [Fudamoto et al. 2017](#); [Zavala et al. 2018](#); [Ma et al. 2019](#); [Bakx et al. 2020](#); [Montaña et al. 2021](#)).

Observations with Atacama Large Millimeter/submillimeter Array (ALMA) and *James Webb Space Observatory* (*JWST*) at resolutions less than 1 arcsecond have shown that, what we considered as extreme red galaxies based on *Herschel* observations, in many cases are galaxies that are being gravitationally amplified or multiple galaxies blended within the *Herschel* large beam. Some of these galaxies and galaxy groups might be interacting galaxies tracing overdense environments, which could be progenitors of elliptical galaxies or the massive galaxy clusters in the local Universe (e.g. [Fudamoto et al. 2017](#); [Oteo et al. 2018](#); [Amvrosiadis et al. 2018](#); [Zavala et al. 2018, 2019](#); [An et al. 2019](#); [Jones et al. 2023](#)).

In this work we compile the currently largest sample of red-*Herschel* galaxies from the *H-ATLAS* with publicly available ~ 1 arcsecond angular resolutions ALMA observations. The high angular resolution data allow us to quantify the relative abundance of single, multiple, and potentially lensed galaxies within this population. Using the SPIRE and ALMA photometry, we further characterize the redshift distribution and physical properties of those red-*Herschel* sources identified as individual galaxies and potentially lensed or close merging systems. The analysis of the *Herschel* sources in our sample identified as multiple systems (i.e. blending two or more ALMA detections) will be presented in a forthcoming paper.

This paper is structured as follows: Section 2 provides a detailed description of the sample selection, data processing and source detection; Section 3 presents the methodology and results; Section 4

compares our results in the framework of the different studies of red-*Herschel* galaxies as in the general scheme of the SMG population; finally, we summarize our results and conclusions in Section 5.

In this work we assume a Λ CDM cosmology using $H_0 = 70\ \text{km s}^{-1}\ \text{Mpc}^{-1}$, $\Omega_M = 0.3$ and $\Omega_\Lambda = 0.7$.

2 DATA AND SAMPLE SELECTION

2.1 Red *H-ATLAS* galaxies observed with ALMA

We build a sample of red *Herschel* galaxies (defined with a simple selection criterion of $S_{250\ \mu\text{m}} < S_{350\ \mu\text{m}} < S_{500\ \mu\text{m}}$) using the data release catalogs from *H-ATLAS* ([Valiante et al. 2016](#); [Maddox et al. 2018](#)). We find 6,194 sources that meet the criterion, representing only 1.4 per cent of all the *H-ATLAS* detections.

We crossmatch our catalog with public data from the ALMA archive using Python Virtual Observatory (PyVo) v1.5.1 and adopting a 5 arcseconds search radius. We find that 3,187 of these red-*Herschel* sources have been observed in 41 public ALMA projects, with 3,257 pointings in band 6, 192 in band 3, 96 in band 4, 18 in band 5, 61 in band 7 and 20 in band 8. Band 6 observations represent 97 per cent (3,089) of the total red *Herschel-ATLAS* sources observed with ALMA². We thus focus our analysis on this Band 6 data-set, which benefits from an homogeneous depth and angular resolution.

2.2 ALMA data

To extract the available data at 1.3 mm (233 GHz), we first obtained the calibrated visibilities or measurement sets (MS) from the NRAO Data Archive³. The standard reduction and calibration of the ALMA pipeline was adopted. Projects such as 2018.1.00526.S (P.I. I. Oteo) take advantage of the ALMA clustering algorithm, which allows for very short observations of less than 1 minute per source thanks to the sharing of calibration observations. This strategy is, however, limited to sources within 10 degrees (or within 1 degree in the case of long-baseline configurations or high-frequency observations) and may not be applicable to other samples.

We then produced the images from the ALMA visibilities using CASA ([Team et al. 2022](#)) and the task `tclean`, which computes the Fourier transform of the *uv* visibilities. In the case of fields with multiple observations, we combine all the available MS files into one single map. First, we create the dirty maps in which we use `Sigma clip` from Astropy v5.3.1 to obtain a global value of the noise r.m.s in the maps. The sigma clipping method removes all the data that have values outside a given threshold, in our case $\pm 5\sigma$.

As a second step for the imaging, we use the `tclean` task to produce clean maps of each field with a clean threshold of 3σ (being 1σ the r.m.s. value of the sigma-clipped dirty map described above). The noise values in the clean maps range from 0.1 to 3.6 mJy beam⁻¹ with median of 0.17 mJy beam⁻¹. Figure 1 shows the distribution of r.m.s. values for those fields with r.m.s. less than 1 mJy. The eight fields with r.m.s. greater than 1 mJy beam⁻¹ were identified as being centered on Active Galactic Nuclei (AGN) in Section 2.3. The

¹ It must be noted, however, that low redshift galaxies with unusually cold temperatures can show a similar shape of their FIR spectrum.

² Projects 2016.1.00087.S (P.I. S. Chapman), 2018.1.00489.S and 2018.1.00526.S (P.I. I. Oteo). The Science Verification Project 2011.0.00017.SV (P.I. ALMA Observatory) includes one additional red-*Herschel* source. This project, however, does not have available data in the NRAO Data Archive.

³ <https://data.nrao.edu/portal/>

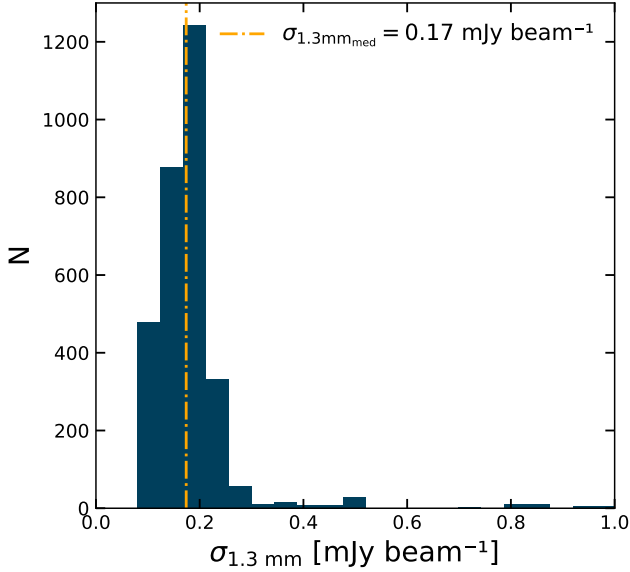


Figure 1. Histogram of the r.m.s. noise of the 1.3 mm ALMA (excluding 8 fields with r.m.s. greater than 1 mJy beam^{-1} identified as AGN). The median r.m.s. of the sample is $0.17 \text{ mJy beam}^{-1}$. Note that the expected 1.3 mm flux density of a red-*Herschel* source with $S_{500\mu\text{m}} \sim 40 \text{ mJy}$ (i.e. the *H-ATLAS* catalog detection limit) is 1.5 mJy , extrapolated using a modified black body at $z = 2$ and with typical SMG values with luminosity-weighted dust temperature

$$T_{\text{dust}} = 30 \text{ K, emissivity index } \beta = 1.8, \text{ and } L_{\text{IR}} = 6 \times 10^{13} L_{\odot}.$$

extremely bright AGN ($\text{SNR} > 100$) detected in these fields limit the dynamical range of the observations introducing artifacts in the maps which increase the measured r.m.s. All the maps have a size of 216×216 pixels, with pixel sizes of $0.14\text{--}0.25$ arcseconds, and are cut to a primary beam response of 0.2 . The beam-sizes range from 0.8 to 1.6 arcseconds and have a mean value of 1 arcsecond. We used a `natural` weighting, which uses uv visibilities with alike data weights in the weight grid following the sample density pattern on the uv -plane, which increases the signal to noise at the expense of a slight lower angular resolution (Remijan et al. 2019). All the pointings together cover an area of $\sim 1,000$ square arcminutes, larger than most of the ALMA blind surveys to search for Dusty Star-Forming Galaxies (DSFG) (e.g. Zavala et al. 2021; Franco et al. 2023).

2.2.1 Source Detection and False Detection Rate

To identify sources in the ALMA data, we make use of the maps that are not corrected by the primary beam response created as described in Section 2.2. These maps have the advantage of having a constant noise, which can be used to easily create signal-to-noise ratio maps.

The detection is performed by searching the maps for pixels that have values above a certain threshold within a radius of 16.6 arcseconds to avoid the noisiest regions at the edges of the map. Within this region, the primary beam response is above 0.3 . When a pixel exceeding this value is identified, we mask a region equal to 1.5 times the beam-size. This process is done iteratively until no more pixels are found over this threshold in a given map.

To calculate the false detection rate (FDR) as a function of signal-to-noise ratio, we first run our detection algorithm with a minimum threshold of 3σ and define these detections as "Positive" (D_P). Then,

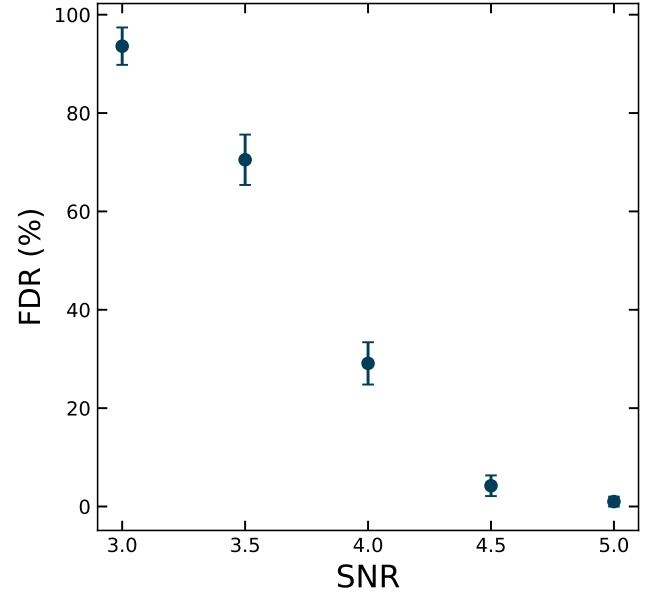


Figure 2. False detection rate (FDR) as a function of SNR, estimate within a 16.6 arcseconds radius to avoid the noisier regions at the edge of the 1.3 mm ALMA maps. We adopt a 5σ detection threshold where the FDR is estimated to be < 1 per cent. The uncertainties of the FDR were estimated through a bootstrap technique with 100 realizations with different random subsamples.

we multiply the maps by -1 and run again the detection algorithm, defining such detections as "False" (D_F) since they are expected to arise only from noise fluctuations. Finally, the FDR is estimated as:

$$\text{FDR}[\%] = \left(\frac{D_F}{D_P} \right) \times 100. \quad (1)$$

This procedure was carried out for different thresholds, as shown in Fig. 2. As it can be seen, at $> 5\sigma$, the FDR drops below ~ 1 per cent. Therefore, to be conservative, in this work we use a 5σ detection threshold. We note that the main results do not change significantly if we adopt a different threshold (e.g. 4.5σ , where the FDR is around 5 per cent).

Using this 5σ threshold, we identify 673 fields with non detections (same number at 4.5σ) and $2,416$ fields with at least one detection. Out of these $2,416$ fields, we found multiplicity in 494 maps, which means that these fields have at least two possible sources detected over 5σ in an area similar to the *Herschel*/SPIRE beam at $500 \mu\text{m}$.

2.2.2 Flux density measurements

For each detected source, we measure the flux density at the brightest pixel and the corresponding value within a given aperture. In the first case, the measured flux density (i.e. brightest pixel value) and its associated uncertainty (σ_p , the standard deviation of the constant-noise map) are corrected by the primary beam response at the position of the detection. For the aperture measurements, we coadd the flux density within different apertures (from 1.5 to 3 times the beam-size) and correct them dividing by the synthesized beam. We adopt the flux density value where its aperture growth curve becomes constant. The uncertainty of the aperture flux density (σ_a) was estimated following equation 2 of Béthermin et al. (2020). After all the corrections were done, we added the calibration uncertainty (σ_{ca}) for ALMA, that is

a around 6 to 10 per cent of the flux density measurement (Remijan et al. 2019). The final value for the uncertainty is given by,

$$\sigma_c = \left(\sigma_{ca}^2 + \sigma_x^2 \right)^{1/2}, \quad (2)$$

using $\sigma_x = \sigma_p$ or σ_a . We adopt $\sigma_{ca} = 0.1$.

2.3 Sample cleaning

We cleaned our sample of contamination from AGN and low-redshift galaxies ($z < 1$) using the The Million Quasars (MILLIQUAS) Catalog (Flesch 2023) and the 17th Data Release of the Sloan Digital Sky Survey (SDSS) (Abdurro'uf et al. 2022).

Any ALMA detection lying at ≤ 2 arcsecond from a source in the MILLIQUAS and SDSS catalogs is considered a match and is therefore discarded from our analysis. We classified 43 ALMA sources as AGN or galaxies at $z < 1$. These sources are presented in Table A1.

2.4 Flux density estimation in SPIRE maps

Taking advantage of the better positional accuracy from the ALMA observations, we re-estimate the SPIRE fluxes in the three different bands using a deblending technique similar to the one presented by Michałowski et al. (2017).

First, we made 120×120 arcseconds² postage stamps from the background subtracted and unfiltered SPIRE maps for each source in our sample, centered at the center of the ALMA maps. Second, to account for the emission from any nearby galaxy around the ALMA position, we searched for $250 \mu\text{m}$ -detected sources (using a 4σ threshold) outside of our ALMA detection radius (16.6 arcsecond). Third, we performed a simultaneous 2D Gaussian fit for each source detected in the postage stamp, including the ALMA detection inside our detection radius and any $250 \mu\text{m}$ source outside this radius.

During the fitting, we fix the FWHM of the Gaussian to the FWHM measured from the Neptune PSF maps and fix the position to that from the ALMA and the $250 \mu\text{m}$ maps. PLUM - Fields are also treated as single sources since the sources found are separated by less than 3 arcsecond, which is smaller than the *Herschel*/SPIRE pixels (6×6 , 8×8 , and 12×12 arcseconds² at 250, 350, and $500 \mu\text{m}$, respectively). In this case, we adopt the position of the brightest component, but we get similar results if the centroid of the sources is adopted. The Gaussian amplitude and the background level are set as free parameters. The fitted Gaussian amplitude represents the final deblended flux density of the source. This process is repeated for each of the three bands, but the search of sources in the outer regions is always based on the $250 \mu\text{m}$ map, which has the best angular resolution. The uncertainties in the fitted amplitudes are used as the flux density errors, which are added in quadrature along with the confusion noise and the absolute calibration errors. The SPIRE maps have a confusion noise of 5.8, 6.3 and 6.8 mJy/beam, respectively and a calibration uncertainty of 5.5 per cent (Valiante et al. 2016).

Our deblending flux densities are compared to the ones from the *H-ATLAS* catalogs in Fig. 3. Overall, there is a very good agreement between the two sets of values, with a small dispersion. The largest difference is at the faint-end of the $500 \mu\text{m}$ flux densities, where our estimations go below the ~ 40 mJy detection limit of *H-ATLAS* (Valiante et al. 2016). Flux densities at $500 \mu\text{m}$ from the *H-ATLAS* catalog are ~ 10 per cent higher than our deblended estimates. If, for a more conservative comparison, only those sources with deblended

flux densities above the *H-ATLAS* detection limit are considered, the $500 \mu\text{m}$ flux densities from the *H-ATLAS* catalogues are ~ 6 and 8 per cent higher than our deblended flux densities for the PLUM - Fields and S - Fields, respectively. This difference may change the number of galaxies classified as red-*Herschel* sources in the sample and have implications in the estimations of redshifts and other properties, as discussed in Section 4.

3 ANALYSIS AND RESULTS

3.1 Classification

Fields with at least one source detected above the adopted threshold (i.e. 2416 fields) were classified in three different groups depending on the number of detections and their proximity. Examples of the three classifications, which are described in detail below, can be found in Fig. 4.

3.1.1 S - Fields

Fields that have only a single detection above 5σ within the 16.6 arcseconds search radius are classified as S - Fields. These are the dominant class with a total of 1,762 sources (1,761 at 4.5σ). The flux density range is 0.78 mJy to 14.74 mJy with a median of 3.14 mJy at 1.3 mm.

3.1.2 PLUM - Fields

Potential Lenses and Unidentified Mergers (PLUM - Fields) are fields with at least two detections separated by no more than 3 arcseconds, which may be lensed systems or closely interacting galaxies. The 3 arcsecond separation was chosen based on the typical separation of strong lenses reported in the literature (e.g. Zavala et al. 2018; Gururajan et al. 2022; Bendo et al. 2022). An additional visual inspection of the whole sample was performed to identify arc-like or extended structures (larger than the synthesized beam) that were originally identified as a single source by our source-detection algorithm, finding 46 such cases.

In total, this category contains 137 fields (149 at $> 4.5\sigma$) after cleaning for AGN and low- z galaxies interlopers. The flux density range is 1.00 mJy to 35.22 mJy with a median of 4.75 mJy at 1.3 mm. From this subsample, we identified 12 fields that are robust lenses confirmed in the literature (Bussmann et al. 2013; Negrello et al. 2016; Fudamoto et al. 2017; Lewis et al. 2018; Manjón-García et al. 2019; Urquhart et al. 2022) or show a strong arc-like morphology in the ALMA observations (supporting their lensed nature; see further discussion in Section 4.1).

3.1.3 M - Fields

Multiple fields include those with two or more sources that are separated by more than 3 arcseconds. This category contains 475 systems. From these, 421 have only two components, 51 have three sources, and 3 fields have 4 detections. The sources in these fields have an average flux density of ~ 2.7 mJy at 1.3 mm. The analysis and physical properties of these fields will be presented in a forthcoming paper.

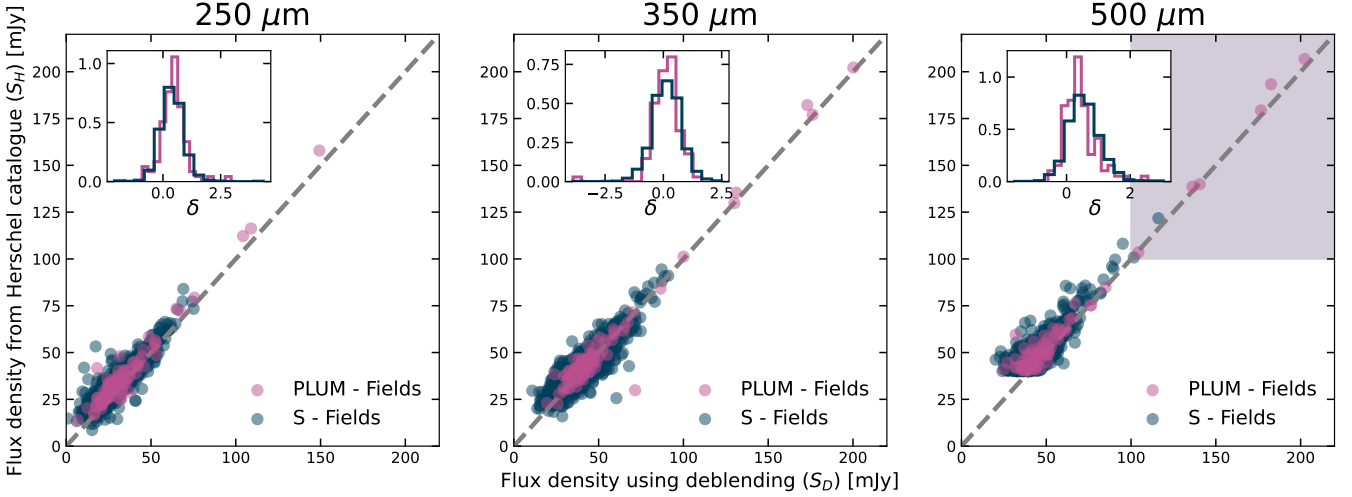


Figure 3. Comparison between the SPIRE fluxes from the *H*-ATLAS catalog (Valiante et al. 2016; Maddox et al. 2018; Ward et al. 2021) and the optimized fluxes obtained in this study. Single sources (S - Field) are shown in blue, while the potential lensed and/or unidentified mergers (PLUM - Fields) are shown in pink. Our fluxes were obtained through a deblending technique (Section 2.4), in which a two-dimensional Gaussian fit was made, fixing the position of the source detected in ALMA and the FWHM to the resolution of the SPIRE map. The shaded region indicates the sources that have fluxes over 100 mJy at 500 μm in both catalogs. Sources above this limit are expected to be gravitationally amplified systems (Negrello et al. 2010), as suggested also by ALMA observations and their PLUM classification (with the exception of two single sources). The inset histograms show a similar scatter of the flux density measurements (in terms of $\delta = (S_H - S_D) / \sigma_D$) for both S - Fields and PLUM - Fields.

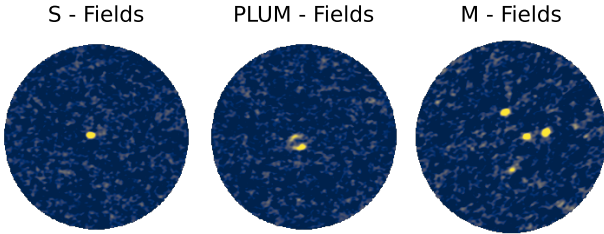


Figure 4. Examples of 1.3 mm ALMA maps for the three subsamples: S - Fields (singles; HATLASJ232147.3-340644 with one detection), PLUM - Fields (potential lenses and unidentified mergers; HATLASJ234350.6-295817 with two arc-like detections) and M - Fields (multiples; HATLAS J122459.1-005647 with four detections). These maps have a radius of ~ 18.6 arcseconds and a median r.m.s. of $0.17 \text{ mJy beam}^{-1}$.

Median	S - Fields	PLUM - Fields
z	2.78 ± 0.03 [2.13-3.43]	3.28 ± 0.12 [2.53-4.09]
$L_{\text{IR}} [10^{12} L_{\odot}]$	(8.9 ± 0.2) [5.3-14]	(13.5 ± 1.2) [8.4-24]
$\text{SFR} [\text{M}_{\odot} \text{yr}^{-1}]$	1300 ± 30 [800-2160]	2000 ± 170 [1240-3590]
$M_{\text{gas}} [10^{11} M_{\odot}]$	(4.1 ± 0.1) [2.6-6.2]	(5.7 ± 0.3) [3.8-9.7]
$M_{\text{dust}} [10^9 M_{\odot}]$	(2.20 ± 0.04) [1.5-3.2]	(3.00 ± 0.20) [2.1-4.9]

Table 1. Median values of the physical properties estimated combining the deblended SPIRE/*Herschel* and ALMA photometry for the S - Fields and PLUM - Fields samples. The uncertainties of the medians were calculated through a bootstrap of 100 synthetic subsamples. The values inside the square brackets indicate the limits containing the 68 per cent of the distributions (i.e. the 16th/84th percentiles).

3.2 Redshifts, Luminosities and Star Formation Rates

We use the software package Millimeter Photometric Redshift (MMPz, Casey 2020) to estimate photometric redshifts and infrared luminosities for the S - Fields and PLUM - Fields samples, using the *Herschel* and ALMA photometry derived in this work. For PLUM - Fields, the total ALMA 1.3 mm flux density is estimated by adding the flux density from individual components with their uncertainties added in quadrature.

This software fits modified black bodies to photometric data-points and obtains the most probable combinations of z_{phot} , L_{IR} and λ_{peak} . The best set of parameters is selected based on the empirical relationship between λ_{peak} and L_{IR} (Casey et al. 2018):

$$\langle \lambda_{\text{peak}}(L_{\text{IR}}) \rangle [\mu\text{m}] = \lambda_0 \left(\frac{L_{\text{IR}} [L_{\odot}]}{L_t} \right)^{\eta}, \quad (3)$$

where $\lambda_0 = 102.8 \pm 0.4 \mu\text{m}$, $L_t = 10^{12} L_{\odot}$ and $\eta = -0.068 \pm 0.001$.

To test the accuracy of this methodology, we compare the photometric redshifts estimated for sources in our samples with available spectroscopic measurements in the literature (Fig. 5). The relative difference between photometric and spectroscopic redshifts ($z_{\text{spec}} - z_{\text{phot}} / (1 + z_{\text{spec}})$) is ~ 8 per cent. Thus, our photometric redshifts are accurate enough for a statistical characterization of this population of galaxies, the main goal of this paper.

Figure 6 shows the redshift probability distribution for the S - Fields and the PLUM - Fields, which have a median redshift of 2.78 ± 0.03 and 3.28 ± 0.12 , respectively. The biased distribution towards higher redshifts of the PLUM-Fields may be reflecting the fact that the probability of strong gravitational lensing increases as a function of redshift (e.g. Hezaveh & Holder 2011; Weiß et al. 2013). A deeper discussion and a comparison with other results from the literature is presented in Section 4.3.

The median L_{IR} of the S - Fields is $8.9 \pm 0.2 \times 10^{12} L_{\odot}$ and for the PLUM - Fields is $13.5 \pm 1.2 \times 10^{12} L_{\odot}$ (see Fig. 7). The larger

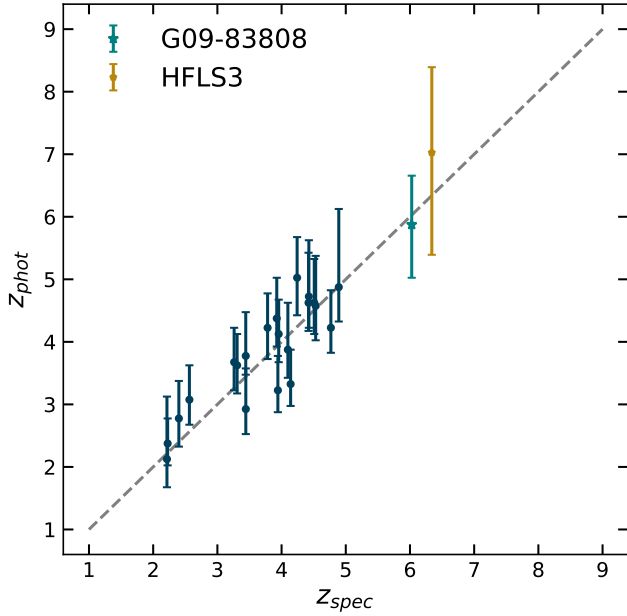


Figure 5. Comparison between the photometric redshifts obtained with MMPz in this work and spectroscopic determinations reported in the literature (Fudamoto et al. 2017; Bakx et al. 2020; Montaña et al. 2021; Urquhart et al. 2022; Cox et al. 2023, and Montaña et al, in prep.). Also included are the starburst galaxies HFLS3 ($z = 6.34$; Riechers et al. 2013) and G09-83808 ($z = 6.027$; Zavala et al. 2018) with their photometric redshifts estimated using MMPz. Their median offset, $(z_{\text{spec}} - z_{\text{phot}})/(1 + z_{\text{spec}}) \approx 0.08$, confirms the reliability of our photometric redshifts to conduct a statistical characterization of the large sample of red-*Herschel* galaxies considered in this work.

L_{IR} values of the PLUM - Fields are expected since this sample includes those sources that are likely amplified by gravitational lensing effects (see, for example, Fig. 10). Although most of the PLUM - Fields have extended detections with arc-like structures, it is also possible that a small fraction of these sources are interacting systems rather than lensed galaxies. If the higher luminosities of some of these sources were intrinsic, this would imply that galaxy interactions might trigger more extreme events of star formation, increasing (at least temporarily) their total IR luminosities.

Finally, we derive star formation rates from the IR luminosities following the relation presented in Kennicutt & Evans (2012), $\text{SFR} [\text{M}_{\odot} \text{yr}^{-1}] = 1.48 \times 10^{-10} L_{\text{IR}} [\text{L}_{\odot}]$, which assumes a Kroupa (2001) IMF. We find a median SFR of $1300 \pm 30 \text{M}_{\odot} \text{yr}^{-1}$ for the S - Fields and $2000 \pm 170 \text{M}_{\odot} \text{yr}^{-1}$ for the PLUM - Fields. These SFR are also indicated in the top axis of the left panel of Fig. 7 and compared with those from other galaxies in Section 4.4.

3.3 Gas and Dust Masses

To infer the gas mass content of the galaxies in our sample, we use the relation given by Scoville et al. (2016), which is calibrated using galaxies with CO line detections and Rayleigh Jeans dust continuum measurements of local star-forming galaxies, low- z ULIGRs and $z \sim 2$ SMG. This method has been previously used in similar studies of high- z SMG (e.g. Harrington et al. 2017; Birkin et al. 2020; Castillo et al. 2023). This relation, which takes advantage of the fact

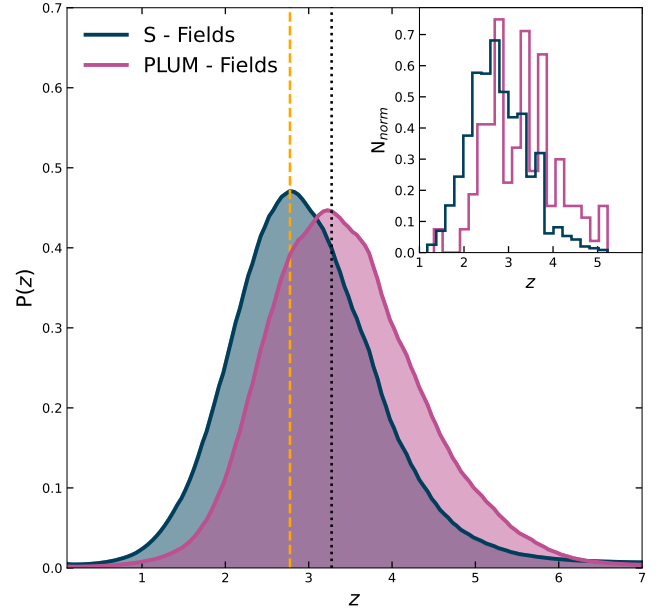


Figure 6. Redshift probability density distributions for S - Fields and PLUM - Fields (solid curves), and histograms of the best-fit photometric redshifts (inset). The median of the S - Fields is marked in yellow (dashed line) and the median for the PLUM - Fields is in black (dotted line). For the PLUM - Fields 60 per cent of the sources are at $z > 3$ while only 35 per cent of the S - Fields lie at these higher redshifts.

that the Rayleigh Jeans regime is optically thin, is given by:

$$M_{\text{gas}} [\text{M}_{\odot}] = 1.78 S_{\nu_{\text{obs}}} [\text{mJy}] (1 + z)^{-4.8} \left(\frac{\nu_{850\mu\text{m}}}{\nu_{\text{obs}}} \right)^{3.8} \times (d_L [\text{Gpc}])^2 \left(\frac{6.17 \times 10^{19}}{\alpha_{850}} \right) \frac{\Gamma_0}{\Gamma_{\text{RJ}}} 10^{10} \text{M}_{\odot}, \quad (4)$$

where $\alpha_{850} = (6.17 \pm 1.7) \times 10^{19} \text{ergs s}^{-1} \text{Hz}^{-1} \text{M}_{\odot}^{-1}$ is a constant derived from the gas mass and the $850 \mu\text{m}$ luminosity, d_L is the luminosity distance at the redshift z , Γ_{RJ} and Γ_0 are corrections due to the difference between the rest frame Planck function and the Rayleigh–Jeans at the source redshift and $z = 0$, respectively. We assume a temperature of 25 K, a common mass-weighted value for the cold molecular gas, and a dust emissivity index $\beta = 1.8$.

We estimate a median M_{gas} of $(4.1 \pm 0.1) \times 10^{11} \text{M}_{\odot}$ for the S - Fields and $(5.7 \pm 0.3) \times 10^{11} \text{M}_{\odot}$ for the PLUM - Fields. Their distributions are shown in the bottom panel of Fig. 7. As a sanity check, we search for galaxies in our sample with CO measurements reported in the literature. For the 21 sources with available (mid-J) CO luminosities (e.g. Fudamoto et al. 2017; Montaña et al. 2021; Berta et al. 2023; Hagimoto et al. 2023), we find a mean ratio of ~ 0.8 between the gas masses estimated in this work and those inferred from the CO line detections. Moreover, studies as Zavala et al. (2022) confirmed the reliability of this relation at higher redshifts based on observations towards a $z \approx 6$ gravitationally lensed dusty star-forming galaxy. Furthermore, Castillo et al. (2023) found that, when the same α_{CO} value is adopted, the gas mass estimates using CO (1-0) and the Scoville et al. (2016) method agree within a factor of 2.

Dust masses are estimated using:

$$M_{\text{dust}} [\text{M}_{\odot}] = \frac{S_{\text{obs}} d_L^2}{(1 + z)k(\nu_{\text{obs}})B(\nu_{\text{obs}}, T_{\text{dust}})}, \quad (5)$$

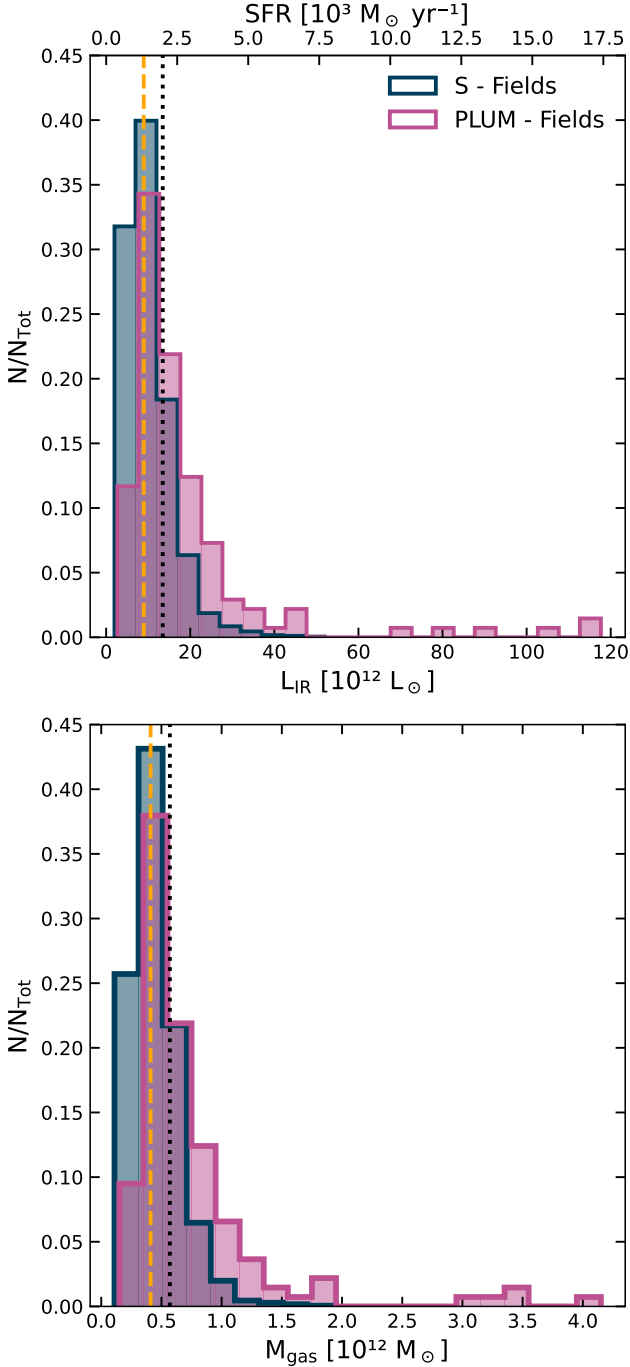


Figure 7. Histograms of the physical properties estimated for the S - Fields and PLUM - Fields samples using 1.3 mm ALMA and deblended *Herschel*/SPIRE photometry: infrared luminosities and SFR (*top*), and gas mass. The median values for the S - Fields are indicated with a yellow dashed line and those for the PLUM - Fields with a black dotted line.

where S_{obs} is the observed flux density at 1.3 mm, d_L is the luminosity distance, z is the redshift (Section 3.2) and $B(\nu_{\text{obs}}, T_{\text{dust}})$ is the Planck function evaluated at the observed frequency ν_{obs} and a mass-weighted dust temperature T_{dust} , for which we adopt a value of 25 K typical of high- z SMG. The mass absorption coefficient $k(\nu_{\text{obs}}) = k_0(\nu_{\text{obs}}/\nu_{850\mu\text{m}})^{\beta}$ is extrapolated from $850\mu\text{m}$ to 1.3

mm assuming $k_0 = 0.07 \text{ m}^2 \text{ kg}^{-1}$ (James et al. 2002) and $\beta = 1.8$. We find median dust masses of $(2.20 \pm 0.04) \times 10^9 M_{\odot}$ for the S - Fields and $(3.00 \pm 0.20) \times 10^9 M_{\odot}$ for the PLUM-Fields.

4 DISCUSSION

In this section we discuss our results within the framework of studies based on smaller samples of red-*Herschel* galaxies and the global context of the SMG population.

4.1 Flux densities and colours

Figure 8 shows a colour-colour plot of our samples of red-*Herschel* galaxies ($S_{250\mu\text{m}} < S_{350\mu\text{m}} < S_{500\mu\text{m}}$), and compares it with the criteria from Ivison et al. (2016, i.e. $S_{500\mu\text{m}}/S_{350\mu\text{m}} \geq 0.85$ and $S_{500\mu\text{m}}/S_{250\mu\text{m}} \geq 1.5$) used to select “ultrared” $z \geq 4$ candidates (e.g. Ivison et al. 2016; Duivenvoorden et al. 2018). This figure shows that, after deblending, 94 per cent of the sources in our sample agree with $S_{500\mu\text{m}}/S_{350\mu\text{m}} \geq 0.85$, while only 45 per cent of the S - Fields and 52 per cent of the PLUM - Fields have $S_{500\mu\text{m}}/S_{250\mu\text{m}} \geq 1.5$. This implies that only 44 per cent of the S - Fields and 51 per cent of the PLUM - Fields meet both conditions. This might explain the relatively small fraction of $z > 3$ sources in our sample — i.e. the original sample selection includes sources that are not as “red” as expected for the highest redshift SMG (although they have similar high luminosities and SFR). This is relatively consistent with the redshifts estimated using MMPz, where 60 per cent of the PLUM - Fields are at $z > 3$.

Negrello et al. (2010), found that sources that have $500\mu\text{m}$ fluxes densities above 100 mJy are expected to be gravitationally amplified (with close to 100 per cent accuracy). This can be further tested thanks to the large sample of red-*Herschel* sources and their 1-arcsec resolution ALMA observations considered in this work. As it can be seen in Fig. 9 (see also Fig. 3), PLUM - Fields indeed dominate at $S_{500\mu\text{m}} \geq 100 \text{ mJy}$, with only two out of the eight sources in this regime cataloged as S - Fields. However, deep higher angular resolution (< 1 arcsecond) data from the ALMA archive (e.g. Projects: 2016.1.00139.S.P.I. R. Ivison and 2021.1.01628.S and 2022.1.00432.S, P.I. T. Bakx) show evidence of strong lensing features in these two sources⁴. This, first, confirms the Negrello et al. criterion to identify lensed systems and, second, implies that we cannot totally discard the possibility that some of the S - Fields are gravitationally amplified sources with no evident lensing features in the ~ 1 arcsecond resolution ALMA images (e.g. Oteo et al. 2017; Bakx et al. 2023).

We therefore explored the possibility of using the 1.3 mm flux density as a criterion for the selection of gravitationally amplified galaxies. As it can be seen in Fig. 9, almost all sources with $S_{1.3\text{mm}} \geq 13.0 \text{ mJy}$ correspond to PLUM - Fields, with the exception of 4 S - Fields. Three of these S - Fields⁵ are clearly gravitationally lensed at higher angular resolution (< 1 arcsecond) ALMA archival data (Projects 2016.1.00139.S, P.I. R. Ivison, 2017.1.00510.S, P.I. I.

⁴ These sources are HARPAS_12 (R.A.: 00h 01m 24.8971s, Dec.: -35 d 42m 12.046s), HARPAS_2444 (R.A.: 22h 42m 07.2143s, Dec.: -32 d 41m 59.480s)

⁵ HARPAS_12 (R.A.: 00h 01m 24.8971s, Dec.: -35 d 42m 12.046s), HARPAS_1789 (R.A.: 13h 33m 37.4892s, Dec.: 24 d 15m 39.326s) and HARPAS_45 (R.A.: 00h 04m 55.4254s, Dec.: -33 d 08m 12.653s)

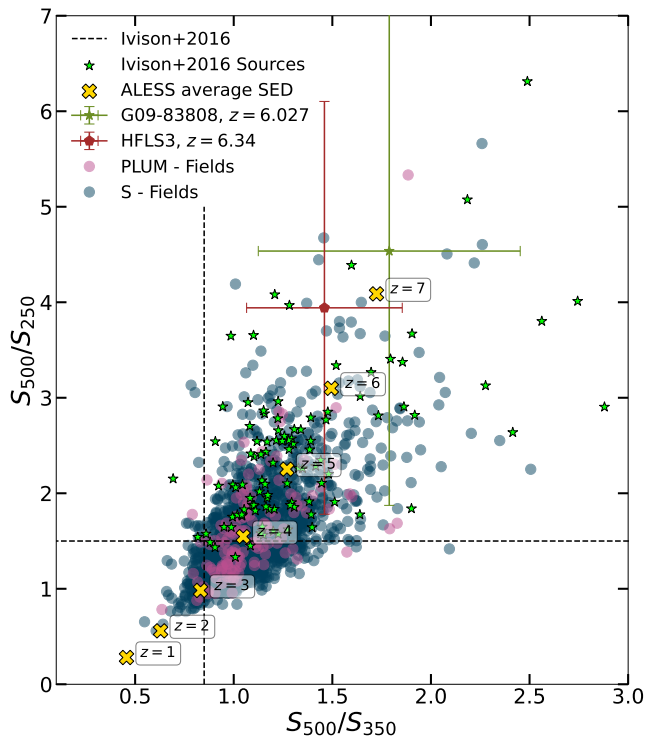


Figure 8. Colour-colour plot (after deblending) of the red-*Herschel* sources in our samples. For comparison, the selection criteria from Ivison et al. (2016) are indicated by the dashed lines, and their sample of “ultra-red” *H-ATLAS* sources (using our deblending technique) are shown as green stars. We find that 44 per cent of the S - Fields and 51 per cent of the PLUM - Fields meet the Ivison et al. (2016) criteria. As a reference, the yellow *x*-symbols indicate the redshift track of a source with a spectral energy distribution corresponding to the averaged template from ALESS (da Cunha et al. 2015). In addition, we show the position of two “ultra-red” *Herschel* sources with spectroscopic redshifts above 6 (Riechers et al. 2013; Zavala et al. 2018)

Oteo, 2021.1.01628.S, P.I. T. Bakx). The fourth source⁶ has CO-line detections (Montaña et al. 2021) and show a factor ~ 10 departure from the L_{CO} -FWHM relation, strongly suggesting it is also gravitationally amplified.

Figure 10 shows all the PLUM - Fields with $S_{1.3\text{mm}} \geq 13.0$ mJy, most of which (if not all) have evident lensing features. Hence we postulate that DSFG with $S_{1.3\text{mm}} \geq 13.0$ mJy are most likely gravitationally amplified. This would also put a strong limit on the maximum luminosity of a dusty galaxy (and thus its SFR), as discussed in Section 4.4.

4.2 Multiplicity

Due to the low resolution of the *Herschel* observations, it is important to understand if the properties estimated for the sources detected in these maps correspond to a single galaxy or are the result of blending multiple galaxies within the same beam. Higher angular resolution observations, e.g. with ALMA and more recently with *JWST*, have confirmed cases of multiplicity in bright *Herschel* sources. The $z = 6.34$ galaxy HFLS3 (Riechers et al. 2013) is a clear example of such

cases, which had long been considered an extreme SMG but *JWST* has recently confirmed to be a high- z interacting system of galaxies (Jones et al. 2023).

Considering the ALMA detections ($\geq 5\sigma$) within the *Herschel* 500 μm beam, we find that 475 out of 2,416 fields (~ 20 per cent) are multiple systems with apparent separations ≥ 3 arc-seconds between components⁷. Of these 475 multiple systems, 87 per cent are doubles, 11 per cent are triples, and 2 per cent have four components. A fraction of these multiple systems may be physically associated galaxies (rather than line-of-sight projections), with some of the denser ones potentially corresponding to galaxy cluster progenitors (similar to those identified by Oteo et al. 2018 and Jones et al. 2023).

Working with samples of similar galaxies (although significantly more limited in size), studies such as Ma et al. (2019), Greenslade et al. (2020), Montaña et al. (2021), and Cox et al. (2023) reported that the multiplicity of the red-*Herschel* sources ranges between 9 and 27 per cent, which is in good agreement with our results. Greenslade et al. (2020) and Montaña et al. (2021) further suggested that, if their non-detections were multiple systems with individual components below the detection limit of the higher angular resolution observations, the multiplicity fraction might increase to $\sim 40 - 50$ per cent. If we assume that the red-*Herschel* sources in our sample undetected in the ALMA 1.3 mm maps are multiple systems, the multiplicity fraction would reach ~ 37 per cent.

4.3 Redshift Distribution

Our results for the S - Fields show that these red-*Herschel* galaxies have a median redshift of 2.78 ± 0.03 , with 68 per cent of the population lying between $z = 2.13$ and 3.43, and a small tail that extends up to redshifts of ~ 6 (Fig. 6). This is a significantly different redshift space compared to that of the general population of *Herschel*/SPIRE selected sources. For example, Casey et al. (2012) presented spectroscopic redshifts for 767 *Herschel* galaxies (selected at 250, 350, and 500 μm from HerMES) with a redshift distribution peaking at $z = 0.85$ and 731 sources at $z < 2$. This highlights that the color selection of red sources within the general *Herschel* population, indeed efficiently filters out the lower redshift ($z < 2$) sources.

Several works have presented photometric-redshift estimations of smaller samples of red-*Herschel* sources, for example: Ivison et al. (2016) studied 109 SMG from the *H-ATLAS* with 850 μm SCUBA-2/JCMT and 870 μm LABOCA/APEX follow-up observations, and estimated a median redshift of 3.6; Ma et al. (2019) compiled a sample of 300 *Herschel* 500 μm -risers with 3.6 and 4.5 μm IRAC/*Spitzer* follow-up and found a median redshift of 3.7. Using a similar color selection to Ivison et al. (2016), Montaña et al. (2021) presented 1.1 mm AzTEC/LMT observations of 100 *H-ATLAS* red galaxies, estimating a median redshift of 3.6.

Compared to our results, these studies show redshift distributions systematically biased towards higher redshifts. This could be attributed to two main reasons: First, as mentioned above, our sample includes galaxies which are not as red as those selected by Ivison et al. (2016). Furthermore, all the sources in our sample are initially detected in the 250 μm band ($\text{SNR} > 2.5\sigma$) and have flux densities above 4σ in at least one of the three SPIRE bands (Valiante et al. 2016; Maddox et al. 2018), while the Ivison et al. (2016) sample includes sources that are not necessarily detected in the shorter-wavelength

⁶ HARPAS_1861 (R.A.: 13 h 39 m 39.9034 s, Dec.: 31 d 22 m 06.672 s); NGP-203484 in Montaña et al. (2021).

⁷ Recall that ALMA detections separated by < 3 arc-seconds are considered single gravitationally lensed galaxies or potential closely interacting systems.

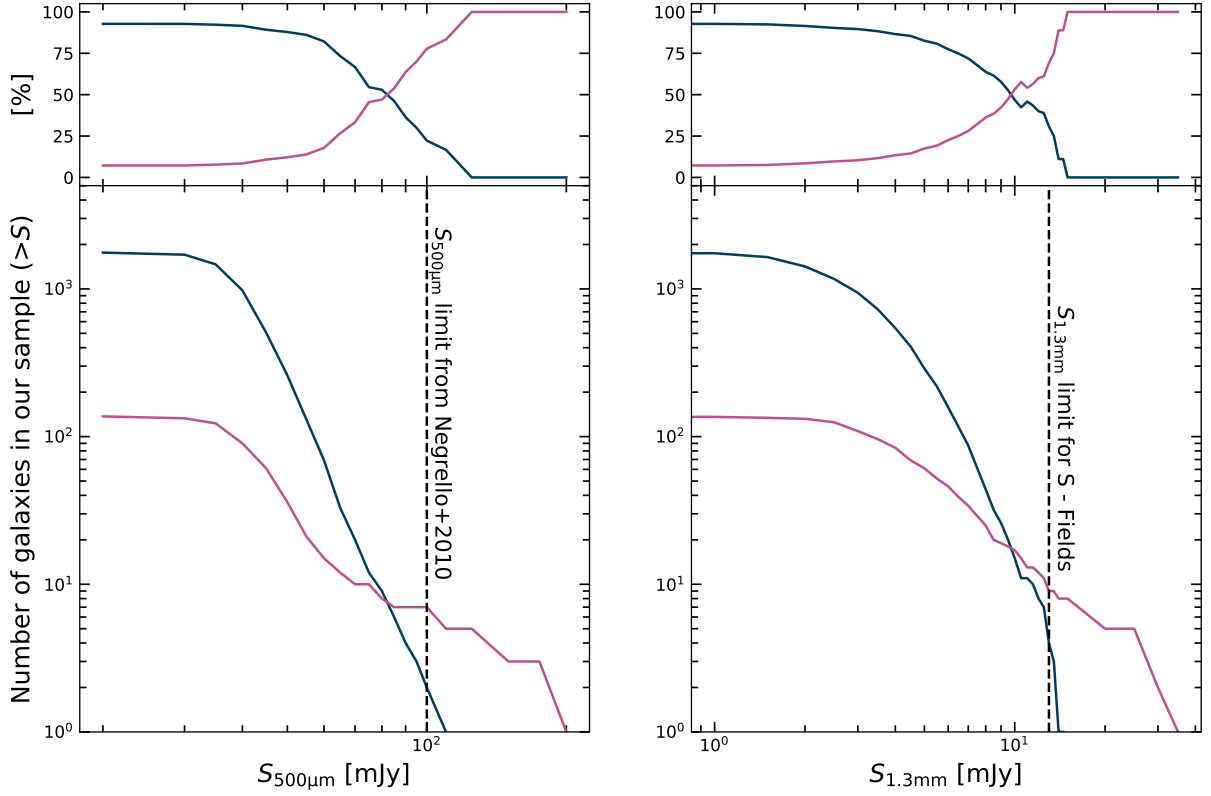


Figure 9. Cumulative number of galaxies in the S - Fields and PLUM - Fields of our sample (*bottom panels*) and their fractional contribution (*top panels*) as a function of $500\mu\text{m}$ (*left*) and 1.3mm (*right*) flux density. The $S_{1.3\text{mm}} \geq 13.0$ is dominated by the PLUM - Fields with only 4 out of the 15 sources above this threshold being S-Fields. Nevertheless, all these 15 sources show evidence of gravitational lensing as discussed in the main text (see also Figure 10). This 1.3mm flux density limit can thus be used to identify DSFG amplified by strong gravitational lensing effects, similar to $S_{500\mu\text{m}}$ limit given by Negrello et al. (2010).

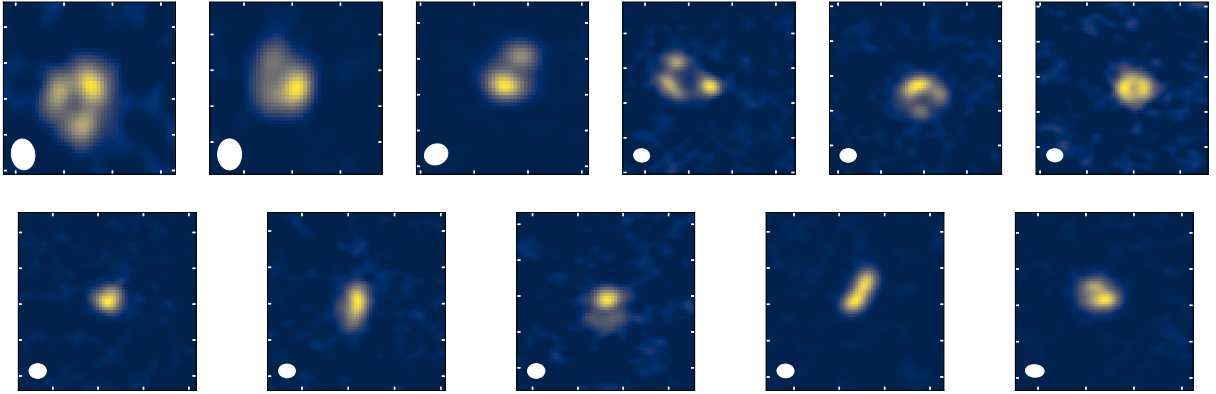


Figure 10. 10×10 square arcseconds postage stamps showing the ALMA 1.3mm observations of all the PLUM - Fields with $S_{1.3\text{mm}} > 13.0\text{mJy}$. The white ellipse represents the synthesized beam (FWHM ~ 1 arcsecond) for each observation. Most of these sources show evident gravitational lensing features. This potentially makes the $S_{1.3\text{mm}} > 13.0\text{mJy}$ limit a selection criterion to identify gravitationally amplified DSFG.

bands, potentially selecting higher redshift galaxies (see BANDFLAGS in Ivison et al. 2016).

Second, the high sensitivity and angular resolution provided by the ALMA observations (compared to previous studies mostly based on single-dish telescope observations) allow us to better constrain the spectral energy distributions and photometric redshifts of these galaxies. Additionally, the different methods used to estimate photometric redshifts might introduce systematic discrepancies between the works. However, as shown in Fig. 5 our photometric redshifts

show a good agreement with the available spectroscopic redshifts for the sample.

Beyond the studies of red-Herschel galaxies, other works have focused on the properties of high- z DSFG selected at longer wavelengths. For example, Simpson et al. (2020) presented ALMA follow-up observations of ~ 180 SCUBA-2 sources with $S_{850\mu\text{m}} > 6.2\text{mJy}$ (i.e. of order $S_{500\mu\text{m}} = 20 - 50\text{mJy}$, the $500\mu\text{m}$ detection limit of our sample), and estimated a median redshift of 2.87 ± 0.08 for their sample. Although dependent on the specific detection limit and selection

wavelength (850 – 1300 μm), different studies of the DSFG population with ALMA have measured redshift distributions with median values between 2.5 and 3, mainly estimated using Optical-FIR photometric redshifts and a few with spectroscopic confirmations (e.g. Hatsukade et al. 2018; Franco et al. 2018; Dudzevičiūtė et al. 2020).

The general agreement between these studies and our estimations suggests that the selection of red-*Herschel* sources overlaps with that of the classic SMG population selected at longer wavelengths, although biased towards higher luminosities (as seen in Fig. 11) due to the shallower depth of the *Herschel* surveys and higher sensitivity to the rarest brightest and highest-redshift systems given the larger areas covered by the *Herschel* blank-field surveys.

For the sample of PLUM - Fields, which are likely dominated by strongly lensed systems (Fig. 10), we estimate a median redshift of 3.28 ± 0.12 , with 83 (i.e. ~ 60 per cent) at $z > 3$. This is slightly higher than the median redshift found for the S-Fields and, as it was previously mentioned, this could be the result of a bias introduced by gravitational lensing effects. Compared to Urquhart et al. (2022), who presented spectroscopic redshifts ($1.41 < z_{\text{spec}} < 4.53$) for 71 gravitationally lensed *Herschel*-galaxies, our sample shows a higher median redshift (3.28 vs 2.75). This is expected since their selection only included sources with $S_{500\mu\text{m}} > 80$ mJy and $z_{\text{phot}} > 2$, without any further color restrictions. On the other hand, Reuter et al. (2020) reported a spectroscopically-derived median redshift of 3.9 ± 0.2 for the 81 strongly gravitationally lensed DSFG in the SPT-SZ Survey, selected at 1.4 mm. This larger value, compared to our estimate for PLUM - Fields, can be attributed to the longer wavelength observations used to select their sample, which are expected to select, on average, higher redshift sources (e.g. Zavala et al. 2014; Béthermin et al. 2015).

4.4 Infrared Luminosities and Star Formation Rates

The infrared luminosities of the S-Fields have a median of $(8.9 \pm 0.2) \times 10^{12} L_{\odot}$. These luminosities are consistent with what is expected for this population and lead to star formation rates of $\sim 1,300 M_{\odot} \text{ yr}^{-1}$. Several studies of red-*Herschel* galaxies in the *H*-ATLAS field find median infrared luminosities between $9 \times 10^{12} L_{\odot}$ and $2 \times 10^{13} L_{\odot}$ (Ivison et al. 2016; Ma et al. 2019; Montaña et al. 2021) with SFR of $\sim 800 - 2,100 M_{\odot} \text{ yr}^{-1}$. Similarly, Greenslade et al. (2020) studied a sample of 34 red-*Herschel* sources from HerMES and found infrared luminosities of $\sim (2 - 6) \times 10^{13} L_{\odot}$. The higher luminosities in these studies might reflect samples biased towards brighter sources, particularly in the case of Greenslade et al. (2020), with a selection criterion of $S_{500\mu\text{m}} > 60$ mJy, compared to > 35 mJy in Ivison et al. (2016); Ma et al. (2019); Montaña et al. (2021), and > 20 mJy in this work (after deblending). Moreover, the studies based on single-dish telescope observations, might be more contaminated by lensed sources than our S-Field sample, that benefits from high angular resolution ALMA data.

Figure 11 shows the L_{IR} (and SFR) of our sources as a function of redshift, and reveals something interesting about the maximum SFR of the sample. We note that all sources with $L_{\text{IR}} \gtrsim 4 \times 10^{13} L_{\odot}$ correspond to PLUM-Fields or can be identified as gravitationally lensed galaxies using high angular resolution (< 1 arcsecond) ALMA archival data (See Section 4.1). This suggests that a single galaxy cannot reach this luminosity levels unless it is gravitationally amplified. In other words, there seems to exist a redshift independent SFR upper limit for SMG around (or below) $\sim 6,000 M_{\odot} \text{ yr}^{-1}$. This is consistent with results from other studies, for example, Barger et al. (2014), using a sample of 850 μm -selected SMG in an area of 400 square arcminutes, found a peak at $\sim 2,000 M_{\odot} \text{ yr}^{-1}$ in the

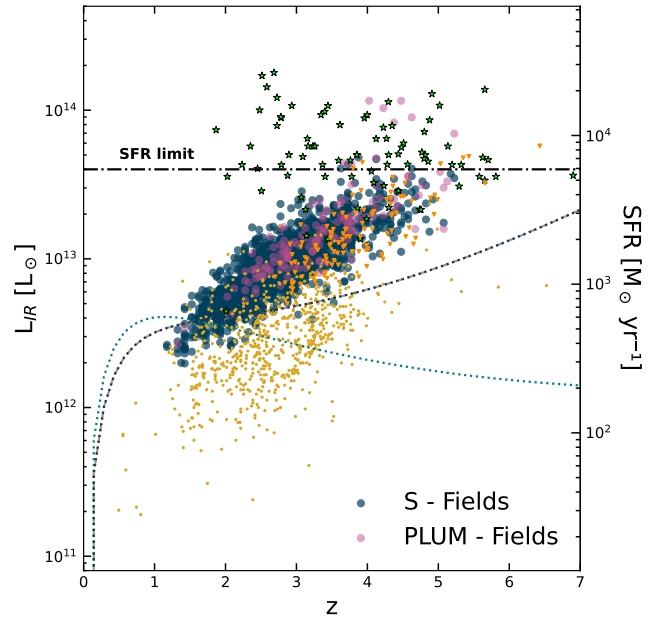


Figure 11. Infrared luminosities (left y-axis) and SFR (right y-axis) of our samples as a function of redshift. PLUM - Fields, being gravitationally amplified or possible close interacting galaxies, reach larger values of L_{IR} at higher redshifts. Yellow dots correspond to ~ 700 SCUBA-2 SMG with ALMA follow-up observations (Dudzevičiūtė et al. 2020). The green stars are ALMA follow-up of 1.4 mm SPT selected sources (not corrected for gravitational lensing amplification, Reuter et al. 2020). To convert L_{FIR} to L_{IR} from Reuter et al. (2020), we use $L_{\text{IR}} \approx 1.3 \times L_{\text{FIR}}$ (Miettinen et al. 2017). Orange triangles correspond to the SCUBA-2 follow-up of “ultra-red” H-ATLAS sources from Ivison et al. (2016). Also shown are the redshift tracks of two modified black bodies with emissivity index $\beta = 2$, dust temperature $T_{\text{dust}} = 45$ K and: $S_{500\mu\text{m}} = 20$ mJy (i.e. lower flux density after deblending, black dotted curve), and $S_{1.3\text{mm}} = 1$ mJy (i.e. our average ALMA $5\sigma_{1.3\text{mm}}$ detection limit, light blue dotted curve). From this figure, an upper limit of $\sim 6,000 M_{\odot} \text{ yr}^{-1}$ (horizontal dot-dashed line) can be established to the SFR of the S-Fields. The nine PLUM - Fields that lie above this limit are shown in Fig. 10.

SFR distribution with values up to $\sim 6,000 M_{\odot} \text{ yr}^{-1}$. Galaxies with reported SFR above this value (e.g. Rowan-Robinson et al. 2018) are, therefore, most likely gravitationally amplified or multiple galaxies blended within a telescope beam. However, this limit only represents a loose constraint (probably being overestimated) since some of the S - Fields might still be contaminated by gravitational lensing.

Finally, we note that 87 S-Fields have $\text{SFR} \gtrsim 3,000 M_{\odot} \text{ yr}^{-1}$. These systems might represent some of the most extreme (unlensed) galaxies found to-date. However, although our sample was cleaned from AGN contamination (Section 2.3), we cannot rule out the possibility that some of these extreme SFR may be overestimated ($\sim 10 - 30$ per cent, Casey et al. 2014) by the presence of a dust obscured AGN. In fact, Rowan-Robinson et al. (2018) found evidence of an AGN in ~ 50 per cent of the 38 *Herschel* extreme starbursts ($\text{SFR} > 5,000 M_{\odot} \text{ yr}^{-1}$) in their sample. In addition some of these extreme galaxies could still be gravitationally lensed or multiple systems not resolved by the 1 arcsecond ALMA resolution, as mentioned above.

4.5 Gas and Dust Mass

As described in Section 3.3, we estimate gas masses we following the method presented in Scoville et al. (2016), which considers optically thin dust continuum emission as a tracer of the interstellar medium mass (see Section 3.3). The medians for our samples are $M_{\text{gas}} = (4.1 \pm 0.1) \times 10^{11} M_{\odot}$ for the S - Fields and $M_{\text{gas}} = (5.7 \pm 0.3) \times 10^{11} M_{\odot}$ for the PLUM - Fields. The galaxies in our sample are therefore massive systems, with large enough gas reservoirs to sustain their high SFR ($\sim 1000 M_{\odot} \text{yr}^{-1}$) for tens and even hundreds of millions years, as discussed below.

Different authors have used direct measurements of CO (1-0), or extrapolations from CO mid-J transitions, to study the molecular gas content in samples of a few to tens of infrared luminous DSFG (e.g. Bothwell et al. 2013; Aravena et al. 2016; Yang et al. 2017; Birkin et al. 2020; Ikarashi et al. 2022; Berta et al. 2023), estimating gas masses of $M_{\text{gas}} \sim 10^{10-11} M_{\odot}$. These values are in broad agreement with the estimates presented in this work, particularly when considering the different methodologies, assumptions on the α_{CO} (typically from 0.8 to 6.5), and different CO line ratios, which could introduce large uncertainties. For example, adopting $\alpha_{\text{CO}} = 1 M_{\odot} (\text{K km s}^{-1} \text{pc}^2)^{-1}$ (a commonly used value for SMG, e.g. Bothwell et al. 2013; Birkin et al. 2020) our gas mass determinations decrease to $M_{\text{gas}} = (6.3 \pm 0.2) \times 10^{10} M_{\odot}$ for the S - Fields and $M_{\text{gas}} = (8.8 \pm 0.5) \times 10^{10} M_{\odot}$ for the PLUM - Fields.

Finally, our dust mass estimations are consistent with massive DSFG at high redshift (e.g. Casey et al. 2019; Ma et al. 2019) with median values of $\sim 10^9 M_{\odot}$. This result confirms the large dust content of these galaxies that obscures most of the star formation activity in this high- z population.

4.6 Depletion times and Star formation efficiencies

The depletion times ($\tau_{\text{dep}} = M_{\text{gas}}/\text{SFR}$), which are independent of gravitational amplification to a first order, can give clues about the processes behind the extreme SFR in these galaxies. We use the values estimated in Sections 3.2 and 3.3 to determine depletion times (and star formation efficiencies (SFE), i.e. $1/\tau_{\text{dep}}$) for the sources in our sample. These results, however, should be taken with caution since the M_{gas} are inferred from the ALMA 1.3 mm photometry and are not totally independent from the SED-based SFR determinations.

The inferred depletion times for the S - Fields cover a range from 0.2 Gyr to 0.4 Gyr. These values are consistent with those found in the literature for similar samples, where the depletion times are between 0.1 Gyr and 1 Gyr (Hatsukade et al. 2015; Pantoni et al. 2021; Berta et al. 2023; Castillo et al. 2023).

On the other hand, our estimated depletion times are lower compared to those found for nearby galaxies ($z < 1$ and $\tau_{\text{dep}} > 1$ Gyr, e.g. Bigiel et al. 2008; Leroy et al. 2008; Genzel et al. 2010). If we scale our gas mass determinations to assume $\alpha_{\text{CO}} = 1 M_{\odot} (\text{K km s}^{-1} \text{pc}^2)^{-1}$, our depletion times are reduced even further (30 to 60 Myr). These values are in agreement with the extreme SMG population reported to have high star formation efficiency (Aravena et al. 2016; Yang et al. 2017; Ikarashi et al. 2022).

Figure 12 shows the depletion times estimated for our samples versus redshift, along with the expected evolution for main-sequence star-forming galaxies and starburst type galaxies (Tacconi et al. 2018). The depletion times of our samples are systematically shorter than those expected for main-sequence galaxies and consistent with the starburst population, showing a mild redshift evolution towards shorter times at higher redshifts.

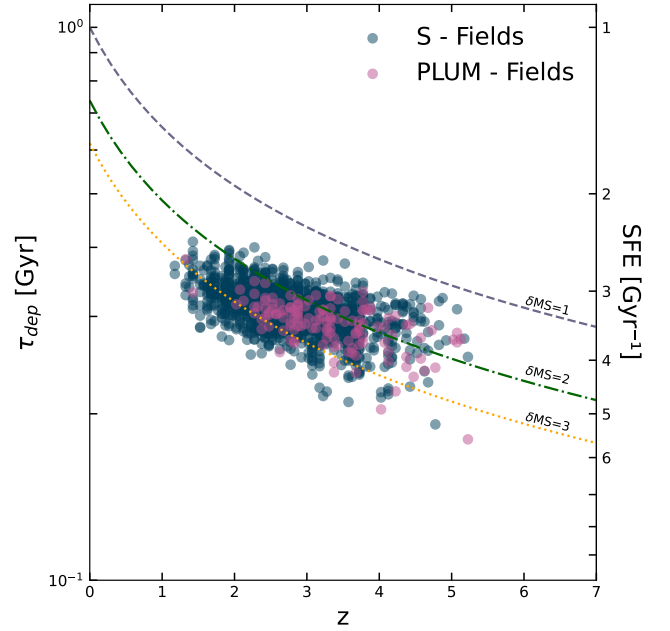


Figure 12. Depletion time (τ_{dep}) as a function of redshift for S - Fields and PLUM - Fields samples. The curves depict the $\tau_{\text{dep}} - z$ relationship (Tacconi et al. 2018) for galaxies in the main sequence ($\delta\text{MS} = 1$, purple dashed curve), and starburst type galaxies $\delta\text{MS} = 2$ (Elbaz et al. 2011, green dash-dot curve) and $\delta\text{MS} = 3$ (Franco et al. 2020, yellow dotted curve). The bulk of our samples has depletion times consistent with a starburst population.

5 SUMMARY AND CONCLUSIONS

Using ALMA archival data at 1.3 mm with 1 arcsecond angular resolution, we studied a sample of $\sim 3,000$ red-Herschel sources selected in the SPIRE/Herschel bands ($S_{250\mu\text{m}} < S_{350\mu\text{m}} < S_{500\mu\text{m}}$). We found 2,416 ALMA maps with detections ($\geq 5\sigma$), of which 1,762 show a single point-like source (S - Fields; 73 per cent), 475 fields with multiple sources (M - Fields; 20 per cent), 137 classified as potential gravitationally lensed or closely interacting systems (PLUM - Fields; 5 per cent), and 43 identified as low- z interlopers or AGN. All sources with $S_{1.3\text{mm}} \geq 13.0 \text{ mJy}$ show features of strong gravitational amplification. This implies a redshift-independent limit of $\sim 6,000 M_{\odot} \text{yr}^{-1}$ to the maximum SFR of SMG and provides a simple photometric criterion to identify lensed systems in future millimeter surveys.

Combining the SPIRE/Herschel photometry with the ALMA band 6 imaging, we conducted an SED fitting analysis and infer the physical properties for the S - Field and PLUM - Field samples. We found a median redshift of 2.78 ± 0.03 for the S - Fields and 3.28 ± 0.12 for the PLUM - Fields. The slightly higher redshift of the PLUM-fields could be attributed to a selection bias, since the probability of a source being gravitationally lensed increases as a function of its redshift. When comparing the redshift distribution of the single sources in our sample with earlier studies of red-Herschel sources, we found that our distribution is shifted towards smaller redshifts. This may be due to the fact that our sample is not as “red” as those presented in previous works which, given the smaller size of their samples, targeted the most extreme sources in terms of color and brightness. The redshift distribution of the red-Herschel sources confirmed to be single systems (i.e. S - Fields) is similar to those estimated for galaxies selected at $850 \mu\text{m}$ or 1.1 mm from single-dish surveys. The

larger area of the *Herschel* surveys, however, increases the probability of identifying the rarest, the brightest, and the highest-redshift systems.

The median IR luminosities for the S - Fields and PLUM - Fields of 8.9×10^{12} and $1.3 \times 10^{13} L_{\odot}$, correspond to SFR of $\sim 1,300$ and $\sim 2,000 M_{\odot} \text{ yr}^{-1}$, respectively. This is in line with previous studies and confirms the extreme nature of these SMG, which also show high gas and dust content with $M_{\text{gas}} \sim 4.9 \times 10^{11} M_{\odot}$ and $M_{\text{dust}} \sim 2.6 \times 10^9 M_{\odot}$. Combining these measurements, we found average depletion times of $\tau_{\text{dep}} = 0.30 \pm 0.03 \text{ Gyr}$, consistent with what has been measured for other SMG, implying high SFE compared to the main-sequence population. Interestingly, the inferred depletion times (and, thus, the SFE) show a mild redshift evolution, consistent with previous result in the literature. We stress, however, that these results should be taken with caution until a more direct measurement of the gas masses become available.

Since most of our sources (~ 73 percent) are individual systems at the current 1 arcsecond resolution, we suggest that the processes increasing the SFE in SMGs act at scales of $\lesssim 8.5 \text{ kpc}$. This rejects early-mergers with separations of several tens of kiloparsecs as the main drivers of the extreme SFR of these galaxies, leaving the door open to mergers near coalescence and other physical processes such as gravitational instabilities and gas turbulence.

These results shed light on the nature of the red-*Herschel* galaxies, which are tracing the most extreme starbursts from the end of the epoch of reionization to cosmic noon. Finally, the legacy catalogs from this work provide excellent targets for follow-up observations aimed at understanding the resolved properties of the most extreme star-forming galaxies and at finding high redshift overdensities of massive dusty galaxies.

ACKNOWLEDGEMENTS

We thank to the anonymous referee for insightful comments that have improved the manuscript. We also want to thank Olga Vega, Yalia Divakara Mayya, Manuel Zamora-Avilés, Elena Terlevich and Eric F. Jiménez-Andrade for their helpful discussions and comments, and to Michał Michałowski for insightful suggestions on the flux-deblending process. MQR would like to thank the Consejo Nacional de Humanidades Ciencias y Tecnologías (CONAHCYT) for her PhD grant. This work has been supported by the CONAHCYT through projects A1-S-45680 and CB 2016 - 281948. JAZ acknowledge funding from JSPS KAKENHI grant number KG23K13150. The *Herschel*-ATLAS is a project from *Herschel*, which is an ESA space observatory with science instruments provided by European-led Principal Investigator consortia and with important participation from NASA. This paper use the following ALMA projects: ADS/JAO.ALMA#2016.1.00087.S, ADS/JAO.ALMA#2016.1.00139.S, ADS/JAO.ALMA#2017.1.00510.S, ADS/JAO.ALMA#2018.1.00489.S, ADS/JAO.ALMA#2018.1.00526.S, ADS/JAO.ALMA#2021.1.01628.S and ADS-JAO.ALMA#2022.1.00432.S. ALMA is a partnership of ESO (representing its member states), NSF (USA), and NINS (Japan), together with NRC (Canada), MOST and ASIAA (Taiwan), and KASI (Republic of Korea), in cooperation with the Republic of Chile. The Joint ALMA Observatory is operated by ESO, AUI/NRAO, and NAOJ. Funding for the Sloan Digital Sky Survey V has been provided by the Alfred P. Sloan Foundation, the Heising-Simons Foundation, the National Science Foundation, and

the Participating Institutions. SDSS acknowledges support and resources from the Center for High-Performance Computing at the University of Utah. SDSS telescopes are located at Apache Point Observatory, funded by the Astrophysical Research Consortium and operated by New Mexico State University, and at Las Campanas Observatory, operated by the Carnegie Institution for Science. The SDSS web site is www.sdss.org. SDSS is managed by the Astrophysical Research Consortium for the Participating Institutions of the SDSS Collaboration, including Caltech, the Carnegie Institution for Science, Chilean National Time Allocation Committee (CNTAC) ratified researchers, The Flatiron Institute, the Gotham Participation Group, Harvard University, Heidelberg University, The Johns Hopkins University, L'Ecole polytechnique fédérale de Lausanne (EPFL), Leibniz-Institut für Astrophysik Potsdam (AIP), Max-Planck-Institut für Astronomie (MPIA Heidelberg), Max-Planck-Institut für Extraterrestrische Physik (MPE), Nanjing University, National Astronomical Observatories of China (NAOC), New Mexico State University, The Ohio State University, Pennsylvania State University, Smithsonian Astrophysical Observatory, Space Telescope Science Institute (STScI), the Stellar Astrophysics Participation Group, Universidad Nacional Autónoma de México, University of Arizona, University of Colorado Boulder, University of Illinois at Urbana-Champaign, University of Toronto, University of Utah, University of Virginia, Yale University, and Yunnan University.

DATA AVAILABILITY

Catalogues are available in supplementary data at MNRAS online. The *Herschel* Astrophysical Terahertz Large Area Survey (*H*-ATLAS) catalogs and maps are available in: <https://www.h-atlas.org/public-data>. The ALMA data band 6 is available in <https://data.nrao.edu/portal/> for the MS files and in <https://almascience.eso.org/aq/> for the maps.

REFERENCES

- Abdurro'uf et al., 2022, *The Astrophysical Journal Supplement Series*, 259, 35
- Amvrosiadis A., et al., 2018, *Monthly Notices of the Royal Astronomical Society*, 483, 4649
- An F. X., et al., 2019, *The Astrophysical Journal*, 886, 48
- Aravena M., et al., 2016, *Monthly Notices of the Royal Astronomical Society*, 457, 4406
- Aretxaga I., Hughes D. H., Dunlop J. S., 2005, *Monthly Notices of the Royal Astronomical Society*, 358, 1240
- Aretxaga I., et al., 2007, *Monthly Notices of the Royal Astronomical Society*, 379, 1571
- Bakx T. J. L. C., et al., 2020, *Monthly Notices of the Royal Astronomical Society*, 496, 2372
- Bakx T. J. L. C., Gray B. S., González-Nuevo J., Bonavera L., Amvrosiadis A., Eales S., Hagimoto M., Serjeant S., 2023, *Monthly Notices of the Royal Astronomical Society*, 527, 8865
- Barger A. J., et al., 2014, *The Astrophysical Journal*, 784, 9
- Bendo G. J., et al., 2022, *Monthly Notices of the Royal Astronomical Society*, 522, 2995
- Berta et al., 2023, *A&A*, 678, A28
- Béthermin et al., 2020, *A&A*, 643, A2
- Bigieli F., Leroy A., Walter F., Brinks E., de Blok W. J. G., Madore B., Thornley M. D., 2008, *The Astronomical Journal*, 136, 2846
- Birkin J. E., et al., 2020, *Monthly Notices of the Royal Astronomical Society*, 501, 3926

- Blain A. W., Smail I., Ivison R. J., Kneib J. P., Frayer D. T., 2002, *Phys. Rep.*, 369, 111
- Bothwell M. S., et al., 2013, *Monthly Notices of the Royal Astronomical Society*, 429, 3047
- Bussmann R. S., et al., 2013, *The Astrophysical Journal*, 779, 25
- B  thermin De Breuck, C Sargent, M Daddi, E 2015, *A&A*, 576, L9
- Carilli C., Walter F., 2013, *Annual Review of Astronomy and Astrophysics*, 51, 105
- Casey C. M., 2020, *The Astrophysical Journal*, 900, 68
- Casey C. M., et al., 2012, *The Astrophysical Journal*, 761, 139
- Casey C. M., Narayanan D., Cooray A., 2014, *Phys. Rep.*, 541, 45
- Casey C. M., et al., 2018, *The Astrophysical Journal*, 862, 77
- Casey C. M., et al., 2019, *The Astrophysical Journal*, 887, 55
- Castillo M. F., et al., 2023, *The Astrophysical Journal*, 945, 128
- Chapman S. C., Blain A. W., Smail I., Ivison R. J., 2005, *The Astrophysical Journal*, 622, 772
- Cox P., et al., 2011, *The Astrophysical Journal*, 740, 63
- Cox et al., 2023, *A&A*, 678, A26
- DaCunha E., et al., 2015, *The Astrophysical Journal*, 806, 110
- Dudzevi  t   U., et al., 2020, *Monthly Notices of the Royal Astronomical Society*, 494, 3828
- Dudzevi  t   U., et al., 2020, *Monthly Notices of the Royal Astronomical Society*, 494, 3828
- Duivendoorden S., et al., 2018, *Monthly Notices of the Royal Astronomical Society*, 477, 1099
- Eales S., et al., 2010, *Publications of the Astronomical Society of the Pacific*, 122, 499
- Elbaz et al., 2011, *A&A*, 533, A119
- Flesch E., 2023, The Million Quasars (Milliquas) catalogue, version 7.10
- Franco et al., 2018, *A&A*, 620, A152
- Franco et al., 2020, *A&A*, 643, A53
- Franco M., et al., 2023, Unveiling the distant Universe: Characterizing $z \geq 9$ Galaxies in the first epoch of COSMOS-Web ([arXiv:2308.00751](https://arxiv.org/abs/2308.00751))
- Fudamoto Y., et al., 2017, *Monthly Notices of the Royal Astronomical Society*, 472, 2028
- Genzel R., et al., 2010, *Monthly Notices of the Royal Astronomical Society*, 407, 2091
- Greenslade J., Clements D. L., Petitpas G., Asboth V., Conley A., P  rez-Fournon I., Riechers D., 2020, *Monthly Notices of the Royal Astronomical Society*, 496, 2315
- Gururajan et al., 2022, *A&A*, 663, A22
- Hagimoto M., et al., 2023, *Monthly Notices of the Royal Astronomical Society*, 521, 5508
- Harrington K. C., et al., 2017, *Monthly Notices of the Royal Astronomical Society*, 471, 4060
- Hatsukade B., Tamura Y., Iono D., Matsuda Y., Hayashi M., Oguri M., 2015, *Publications of the Astronomical Society of Japan*, 67, 93
- Hatsukade B., et al., 2018, *Publications of the Astronomical Society of Japan*, 70, 105
- Hezaveh Y. D., Holder G. P., 2011, *The Astrophysical Journal*, 734, 52
- Hughes D. H., et al., 1998, *Nature*, 394, 241
- Hughes D. H., et al., 2002, *Monthly Notices of the Royal Astronomical Society*, 335, 871
- Ikarashi Ivison, R. J. Cowley, W. I. Kohno, K. 2022, *A&A*, 659, A154
- Ivison R. J., et al., 2016, *The Astrophysical Journal*, 832, 78
- James A., Dunne L., Eales S., Edmunds M. G., 2002, *Monthly Notices of the Royal Astronomical Society*, 335, 753
- Jones G. C., et al., 2023, GA-NIFS: JWST/NIRSpec IFU observations of HFLS3 reveal a dense galaxy group at z 6.3 ([arXiv:2308.16620](https://arxiv.org/abs/2308.16620))
- Kennicutt R. C., Evans N. J., 2012, *Annual Review of Astronomy and Astrophysics*, 50, 531
- Kroupa P., 2001, *Monthly Notices of the Royal Astronomical Society*, 322, 231
- Leroy A. K., Walter F., Brinks E., Bigiel F., de Blok W. J. G., Madore B., Thornley M. D., 2008, *The Astronomical Journal*, 136, 2782
- Lewis A. J. R., et al., 2018, *The Astrophysical Journal*, 862, 96
- Ma J., et al., 2019, *The Astrophysical Journal Supplement Series*, 244, 30
- Maddox S. J., et al., 2018, *The Astrophysical Journal Supplement Series*, 236, 30
- Manj  n-Garc  a Herranz, D. Diego, J. M. Bonavera, L. Gonz  lez-Nuevo, J. 2019, *A&A*, 622, A106
- Micha  owski M. J., et al., 2017, *Monthly Notices of the Royal Astronomical Society*, 469, 492
- Miettinen et al., 2017, *A&A*, 606, A17
- Monta  a A., et al., 2021, *Monthly Notices of the Royal Astronomical Society*, 505, 5260
- Negrello M., et al., 2010, *science*, 330, 800
- Negrello M., et al., 2016, *Monthly Notices of the Royal Astronomical Society*, 465, 3558
- Oteo I., et al., 2016, *The Astrophysical Journal*, 827, 34
- Oteo I., et al., 2017, Witnessing the birth of the red sequence: the physical scale and morphology of dust emission in hyper-luminous starbursts in the early Universe ([arXiv:1709.04191](https://arxiv.org/abs/1709.04191))
- Oteo I., et al., 2018, *The Astrophysical Journal*, 856, 72
- Pantoni L., et al., 2021, *Monthly Notices of the Royal Astronomical Society*, 504, 928
- Pope A., Chary R.-R., 2010, *The Astrophysical Journal*, 715, L171
- Remijan A., et al., 2019, ALMA Doc, 7.3, ver. 1.0
- Reuter C., et al., 2020, *The Astrophysical Journal*, 902, 78
- Riechers D. A., et al., 2013, *Nature*, 496, 329
- Rowan-Robinson et al., 2018, *A&A*, 619, A169
- Saintonge A., et al., 2011, *Monthly Notices of the Royal Astronomical Society*, 415, 61
- Scoville N., et al., 2016, *The Astrophysical Journal*, 820, 83
- Simpson J. M., et al., 2020, *Monthly Notices of the Royal Astronomical Society*, 495, 3409
- Smail I., Ivison R. J., Blain A. W., 1997, *The Astrophysical Journal*, 490, L5
- Tacconi L., et al., 2010, *Nature*, 463, 781
- Tacconi L. J., et al., 2018, *The Astrophysical Journal*, 853, 179
- Team T. C., et al., 2022, *Publications of the Astronomical Society of the Pacific*, 134, 114501
- Urquhart S. A., et al., 2022, *Monthly Notices of the Royal Astronomical Society*, 511, 3017
- Valiante E., et al., 2016, *Monthly Notices of the Royal Astronomical Society*, 462, 3146
- Ward B. A., et al., 2021, *Monthly Notices of the Royal Astronomical Society*, 510, 2261
- We    A., et al., 2013, *The Astrophysical Journal*, 767, 88
- Yang et al., 2017, *A&A*, 608, A144
- Yun M. S., et al., 2012, *Monthly Notices of the Royal Astronomical Society*, 420, 957
- Zavala J. A., Aretxaga I., Hughes D. H., 2014, *Monthly Notices of the Royal Astronomical Society*, 443, 2384
- Zavala J. A., et al., 2018, *Nature Astronomy*, 2, 56
- Zavala J. A., et al., 2019, *The Astrophysical Journal*, 887, 183
- Zavala J. A., et al., 2021, *The Astrophysical Journal*, 909, 165
- Zavala J. A., et al., 2022, *The Astrophysical Journal*, 933, 242
- da Cunha E., et al., 2015, *The Astrophysical Journal*, 806, 110

APPENDIX A: SOURCES CLASSIFIED AS ACTIVE GALACTIC NUCLEI AND LOW-REDSHIFT GALAXIES

Table A1 lists the 43 fields removed from our sample due to their association with Active Galactic Nuclei (86 per cent) and low- z galaxies (14 per cent) using the MILLIQUAS and the 17th Data Release of the Sloan Digital Sky Survey. These fields represent only 2 per cent of the total sample of red H -ATLAS sources identified in the public ALMA archive.

This paper has been typeset from a \LaTeX file prepared by the author.

IAU Name	Type	Catalog	Catalogs Names	R.A.	Dec.	z
HATLASJ000106.6-320638	AGN	MILLIQUAS	2QZ J000106.9-320642	0.277693	-32.110526	
HATLASJ005802.3-323420	AGN	MILLIQUAS	PKS 0055-328	14.509378	-32.572155	
HATLASJ014310.0-320056	AGN	MILLIQUAS	PKS 0140-322	25.791662	-32.015671	0.372
HATLASJ014503.4-273333	AGN	MILLIQUAS	PKS 0142-278	26.263985	-27.559147	
HATLASJ084924.5+014712	AGN	MILLIQUAS	SDSS J084924.52+014713.1	132.352127	1.786842	
HATLASJ090910.1+012134	AGN	MILLIQUAS	PKS 0906+01	137.292358	1.359685	
HATLASJ090940.2+020004	AGN*	NED	PKS 0907+022	137.417755	2.001126	1.601
HATLASJ113320.2+004053	AGN	MILLIQUAS	PKS 1130+009	173.334182	0.681598	
HATLASJ092654.4-002149	AGN	MILLIQUAS	PKS 1148-00	177.681732	-0.398445	
HATLASJ120741.7-010636	AGN	MILLIQUAS	PKS 1205-008	181.923797	-1.110082	
HATLASJ121758.7-002946	AGN	MILLIQUAS	PKS 1215-002	184.494980	-0.496351	0.419
HATLASJ125346.9+232733	AGN	MILLIQUAS	SDSS J125347.08+232726.8	193.445602	23.459068	
HATLASJ125516.4+281827	AGN	MILLIQUAS	SDSS J125516.40+281828.0	193.818436	28.307546	
HATLASJ125728.1+292711	AGN	MILLIQUAS	SDSS J125728.05+292715.1	194.367233	29.453180	
HATLASJ125757.3+322930	AGN	MILLIQUAS	B2 1215+32	194.488815	32.491760	0.806
HATLASJ130129.0+333703	AGN	MILLIQUAS	5C 12.170	195.370910	33.617420	
HATLASJ131028.7+322044	AGN	MILLIQUAS	B2 1308+32	197.619659	32.345508	0.998
HATLASJ131059.2+323331	AGN	MILLIQUAS	MG J1310+3233	197.746750	32.558670	
HATLASJ131736.4+342518	AGN	MILLIQUAS	B2 1315+34A	199.401718	34.421684	
HATLASJ131947.3+292640	AGN	MILLIQUAS	SDSS J131946.93+292640.4	199.947204	29.444395	
HATLASJ132952.9+315410	AGN	MILLIQUAS	87GB 13275+3209	202.4702604	31.902751	
HATLASJ133038.1+250901	AGN	MILLIQUAS	3C 287.0	202.658569	25.150234	
HATLASJ133108.4+303034	AGN	MILLIQUAS	3C 286.0	202.785171	30.509453	0.85
HATLASJ133120.4+291200	AGN	MILLIQUAS	SDSS J133120.40+291200.6	202.835144	29.199993	
HATLASJ133307.4+272518	AGN	MILLIQUAS	CGRaBS J1333+2725	203.280807	27.421665	0.731
HATLASJ134131.1+235043	AGN	MILLIQUAS	SDSS J134131.14+235043.3	205.379699	23.845237	
HATLASJ134208.4+270933	AGN	MILLIQUAS	RRS IV 4	205.535141	27.159134	
HATLASJ140729.5+011216	AGN	MILLIQUAS	SDSS J140729.39+011218.5	211.873001	1.204640	
HATLASJ141004.7+020306	AGN	MILLIQUAS	PKS 1407+022	212.519637	2.0518739	
HATLASJ142121.3-001136	AGN	MILLIQUAS	SDSS J142121.54-001138.9	215.339096	-0.193460	
HATLASJ144424.5-004454	AGN	MILLIQUAS	SDSS J144424.04-004454.5	221.102218	-0.748408	
HATLASJ145146.1+010608	AGN	MILLIQUAS	MASIV J1451+0106	222.942489	1.102491	
HATLASJ222321.6-313701	AGN	MILLIQUAS	J222321.63-313702.1	335.839965	-31.616873	
HATLASJ224838.6-323551	AGN	MILLIQUAS	PKS 2245-328	342.160827	-32.597446	
HATLASJ231859.8-294738	AGN	MILLIQUAS	2QZ J231859.9-294736	349.749207	-29.793848	
HATLASJ235935.3-313343	AGN	MILLIQUAS	PKS 2357-318	359.897247	-31.562063	0.991
HATLASJ131911.4+312732	Low-z galaxy	SDSS	J131911.29+312725.4	199.797500	31.458898	0.256
HATLASJ132545.8+264126	Star*	NED	J132545.54+264123.6	201.440674	26.690624	
HATLASJ134339.0+352335	Low-z galaxy	SDSS	J134338.97+352337.3	205.91231	35.392933	0.2
HATLASJ134857.9+245357	Low-z galaxy	SDSS	J134857.90+245356.4	207.24115	24.899031	0.6
HATLASJ142111.9-013845	Low-z galaxy	SDSS	J142111.98-013843.9	215.299987	-1.646102	0.279
HATLASJ234758.4-331918	Low-z galaxy	SDSS	TGS492Z213	356.993225	-33.321781	0.21

*Classified by NASA/IPAC Extragalactic Database.

Table A1. Fields from our sample that match (at ≤ 2 arcsecond) a source in the The Million Quasars (MILLIQUAS) Catalog (Flesch 2023) and the 17th Data Release of the Sloan Digital Sky Survey (SDSS, Abdurro'uf et al. 2022). Columns 5 and 6 are the coordinates of ALMA maps centers.